Assessment of the electrodeposition synthesized manganese chromite and cobalt-nickel layered double hydroxide composite for high-performance supercapacitor applications

Gift Rutavi, Delvina Japhet Tarimo, Vusani Muswa Maphiri, Vianney Ngoyi Kitenge and Ncholu Manyala*

Department of Physics, Institute of Applied Materials, SARChI in Carbon Technology and Materials, University of Pretoria 0028, South Africa

*Corresponding author's email: ncholu.manyala@up.ac.za, Tel.: + (27)12 420 3549.

Abstract

Cyclic voltammetry (CV) electrodeposition synthesis was performed twice to synthesize manganese chromite ($MnCr_2O_4$-ϕ) on NF, where $-1.4 \leq \phi \leq -1.0$ is the lower voltage (V vs Ag/AgCl) set in the CV during electrodeposition, the higher potential being 0.5 V. This was followed by another electrodeposition of cobalt nickel layered double hydroxide (CoNi-LDH) on $MnCr_2O_4$-ϕ. The unique layered structure of CoNi-LDH produce electrodes with excellent electrochemical performance. $MnCr_2O_4$-1.2 V@CoNi-LDH ($\phi = -1.2$ (V vs Ag/AgCl)) yielded the best electrochemical performance in three-electrode set-up in 2 M KOH with the highest specific capacity of 1529.3 C g^{-1} at a specific current of 1 A g^{-1}. This electrode was incorporated into the hybrid device with activated carbon (AC) from Amarula Husk as the negative electrode (AMH). The device ($MnCr_2O_4$ -1.2 V@CoNi-LDH//AMH) produced a superb specific energy of 80.2 Wh kg^{-1} corresponding to a specific power of 1117.7 W kg^{-1} at 1 A g^{-1}. The device also showed the capacity retention and Coulombic efficiency of the device were 72.9 and 99.7%, respectively after 15 000 GCD cycles at 9 A g^{-1}. Due to the phenomenal performance, the produced materials are suitable candidates for high energy supercapacitor applications.

Keywords: Electrodeposition potential; Manganese chromite; Specific capacity; Supercapacitor; Specific energy.

1.0 Introduction

Supercapacitors have the potential to play a role in facilitating the shift from fossil fuels reliance to cleaner renewable energy sources [1]. This is due to their attractive features such as high specific power, long cycle and life rapid charge-discharge [2–4]. Nevertheless, the specific energy of supercapacitors is still much inferior to that of lithium ion batteries (LIBs). It is essential therefore to source for and investigate affordable and environmentally friendly electrode materials and optimise their synthesis with an intention to improve their specific energy while not compromising their specific power.

Bimetallic metal oxide (BMO) and hydroxide (BMOH) have charge storage mechanisms which are dominated by Faradaic redox reactions produces [5–7]. BMO also avail multiple redox reactions resulting in improved diffusion phenomena which lead to great electrochemical properties [8]. This gives them superior specific capacity and specific energy when compared to carbon based material whose energy storage mechanism is electrostatic without chemical reactions [9–11].

Besides, natural abundance and environmental friendliness, bimetallic metal oxides (BMO) such as $CoFe_2O_4$, $CuFeS_2$, and $NiCo_2O_4$ have generated a lot of interest recently among researchers for supercapacitor electrodes applications because of various valence of cations and the low activation energy for electron transport among the cations of dual metal compounds. The electrical conductivities of BMO are significantly higher than those for single metal oxides [12,13]. BMO also benefits from possessing more electroactive sites compared to monometallic oxides due to the presence of a pair of distinct metals, this goes a long way in improving the electrical conductivity, and electrochemical stability [14–16]. Manganese

chromite ($MnCr_2O_4$) has found regular use in photocatalysts, ceramic dyes, alkaline batteries and water purification due to its structural, magnetic and electrical properties [17]. However, there are very few reports of $MnCr_2O_4$ used in supercapacitors despite its favourable features such as high theoretical specific capacity, structural stability and high electrical conductivity [18,19].

On the other hand, $MnCr_2O_4$ like most BMO, has lower cycle life compared to carbon based materials [20]. The electrochemical accomplishments of $MnCr_2O_4$ can be greatly enhanced by crafting a composite with layered materials. Two dimensional layered materials allow abundant exposed active sites for more rapid ion diffusion during reduction and oxidation processes [21]. Due to its unique and tunable two dimensional layered structure with large interlayer spaces which results in adjustable chemical composition and high anion exchangeability [22–24], cobalt nickel layered double hydroxide (CoNi-LDH) is capable of yielding an elevated theoretical capacitance of 3000 F g^{-1} [25]. CoNi-LDH however suffer from slow electron transport [26,27]and its electroactive sites are confined. The composite of $MnCr_2O_4$ and CoNi-LDH will benefit from the synergetic effect with $MnCr_2O_4$ compensating CoNi-LDH's low electrical conductivity while CoNi-LDH introduce flexible ion interchangeability [22]. For instance, El-Deen et al. successfully synthesized a 3D hierarchical Ni-Co LDH wrapped around porous Co_3O_4 nanotubes derived from (zeolite imidazolate framework-67) ZIF-67 as a template. The composite electrode nickel cobalt layered double hydroxide cobalt oxide nanocomposite (Ni-Co LDH@Co_3O_4) attained a phenomenal specific capacitance of 1866 F g^{-1} at 2 A g^{-1}. This was significantly superior compared to the specific capacitance of 487 and 1161 F g^{-1} produced by the individual electrodes Co_3O_4 and Ni-Co LDH, respectively [28]. Also, Xu et al. used a facile microwave-assisted hydrothermal method to synthesize a sandwich-like cobalt nickel sulfides@carbon@nickel cobalt double hydroxide ($CoNi_2S_4$@C@NiCo-LDH). The nanostructured composite electrode generated a great

performance with an excellent specific capacity of 4259.7 C g^{-1} at 1 A g^{-1} and a huge capacity retention of 85.8 % at 20 A g^{-1}. These are testimonies for the benefits of a composite made from CoNi-LDH with a BMO (spinel) material [29].

Furthermore, the electrical performance and mechanical stability of this material is greatly influenced by the synthesis route [30]. Directly growing electroactive materials onto the surface of a porous substrates such nickel foam is remarkably effective in not only reducing the particles aggregation but also improving the rapid electron transport between the current collector and the active materials, this significantly increases utilisation of electroactive particles [31]. Electrodeposition, which is a cost effective, efficient, facile and safe is one of the most suitable methods for growing materials onto a current collector. As a binder-free route it does not introduce resistivity to the electrode material, and this helps to increase the maximum specific power of the device. Modification of electrodeposition parameters like concentration, precursor solution, pH, current, voltage, number of CV cycles and electrodeposition duration (time) has great effects on the performance of supercapacitor electrode materials [32]. These effects include change in the features of the deposited materials like thickness, surface morphology and conductivity [33–35]. For instance, Zhang et al. were able to improve the specific capacitance of MnO_2 from a general value which is less than 300 F g^{-1} at 1 A g^{-1} to a great value of 469 F g^{-1} at the same specific current by adjusting the electrodeposition potential to 0.6 V vs Ag/AgCl. The electrode also exhibited stability yielding a capacitance retention of 83.9 % after 2,500 cycles [36]. Yavuz et al. explored the influence of cathodic deposition potential on the performance of a cobalt based film [37]. A peak specific capacitance of 1692 F g^{-1} with a capacitance retention of 81 % was obtained when the film was deposited at a voltage of -1.7 V vs Ag/AgCl on a graphite electrode. The investigation also showed that the charge storage mechanism evolved with the deposition voltage with surface controlled reaction began to manifest at a deposition voltage of -1.3 V vs Ag/AgCl. These

finding shows the important role played by the electrodeposition voltage on the electrochemical performance and stability of supercapacitor electrodes.

In this report, successive electrodeposition was employed. The process started with the CV electrodeposition, of $MnCr_2O_4$-ϕ on nickel foam, where ϕ is the electrodeposition potential (V), and the values of ϕ were, -1.0, -1.2 and -1.4 V. The electrode synthesized using -1.2 V ($MnCr_2O_4$-1.2 V) yielded the best electrochemical results and was therefore used to make the composite electrode. The composite electrode ($MnCr_2O_4$-1.2 V@CoNi-LDH) was synthesised through a further CV electrodeposition of CoNi-LDH on $MnCr_2O_4$-1.2 V.

The $MnCr_2O_4$-1.2V@CoNi-LDH electrode produced excellent electrochemical performance in 2 M KOH electrolyte in a three-electrode set-up with a great specific capacity of 1529.3 C g^{-1} at 1 A g^{-1}. The electrode also exhibited excellent stability yielding a capacity retention of 73.6 % and a coulombic efficiency of 99.9 % after 5,000 cycles at a specific current of 8 A g^{-1}. The electrode was incorporated into an asymmetric device ($MnCr_2O_4$-1.2 V@CoNi-LDH//AMH) with AMH as the negative electrode in 2 M KOH. The device yielded a remarkable specific energy of 80.2 Wh kg^{-1} and a specific power of 1117.7 W kg^{-1} at 1 A g^{-1}. The capacity retention and coulombic efficiency of the device at 10,000 GCD cycles at 9 A g^{-1} were 72.9 and 99.7 %, respectively. The study successfully presents a sustainable way of fusing different materials using one simple, efficient, cost effective route while yielding very competitive electrochemical results. This avails the synthesised material as candidate for high yield supercapacitor devices.

2.0 Experimental section

2.1 Materials

There was no further purification performed on the chemicals used. The following are the chemicals used in this study: Nickel foam [NF] was acquired from Alantum (Munich, Germany). Deionised water [DW] was drawn from the DRAWELL water refining device. Hydrochloric acid [HCl] (purity 32 %) acetone [$(CH_3)_2CO$] (purity > 99 %), and ethanol [CH_3CH_2OH] (purity 99.9 %) were all purchased from (Sigma Aldrich, Steinheim, Germany). Chromium(III) potassium sulphate dodecahydrate [$KCr_2(SO_4).12\ H_2O$] (purity ≥ 99 %), manganese acetate hexahydrate [$Mn(CH_3CO_2)_2.4\ H_2O$] (purity ≥ 99 %), sodium sulphate [Na_2SO_4] (purity ≥ 99 %), Nickel nitrate hexahydrate [$Ni\ (NO_3)_2•6H_2O$] (purity 99 %), cobalt nitrate hexahydrate [$Co(NO_3)_2•6H_2O$] (purity ≥ 99 %) were all obtained from Merck (Johannesburg, South Africa) [38–40].

2.2 Preparation of NF substrates

The treatment of NF was performed according to the procedure described in our prior work [41]. This rigorous chemical treatment served to exclude the inert oxide and hydroxide layers which form on the surface of NF in a moist environment. In summary, NF was reshaped into rectangular pieces with (2 cm x 1 cm) dimensions. These pieces were immersed into 3 M HCl for 20 minutes. The pieces were then dipped in acetone, followed by 99% purity ethanol and finally DW, all for 20 minutes. This process was followed by drying at 60^o C in an oven for 12 hours.

2.3 Preparation of $MnCr_2O_4$-ϕ on NF electrode

0.01 M each of [$KCr_2(SO_4).12\ H_2O$] and [$Mn(CH_3CO_2)_2.4\ H_2O$] were added to 500 ml DW and stirred for 30 minutes. 0.01 M Na_2SO_4 was then added to prevent aggregation and the

stirring continued for a further 45 minutes. This solution was identified as S1. To perform the electrodeposition, the Bio-logic workstation was used, with NF, platinum rod, and Ag/AgCl serving as the working electrode (WE), counter electrode (CE) and reference electrode (RE), respectively, these were all dipped in S1. Cycling voltammetry (CV) at 2.5 mV s^{-1} was used in a voltage range of -1.0 to 0.5 V vs Ag/AgCl. The voltage was repeated for voltage ranges -1.2 to 0.5 V vs Ag/AgCl and -1.4 to 0.5 V vs Ag/AgCl. The electrodes were then washed in deionised water (DW) and dried in an oven at 90^{o} C for 8 hours. To transform the phase of the electrode materials from LDH to the spinel phase, the electrodes were then annealed in air for 2 hours at 300^{o}C. The electrodes were labelled as $MnCr_2O_4$-1.0 V, $MnCr_2O_4$-1.2 V, and $MnCr_2O_4$-1.4 V, according to their lower electrodeposition voltage value, ($\phi = -1.0, 1.2$ and $-$ 1.4 V. The mass loading of the synthesized electrodes of the loading were 0.9, 1.1 and 1.2 mg respectively [42–44].

2.4 Synthesis of CoNi-LDH, $MnCr_2O_4$-1.2 V@CoNi-LDH and AMH

The details of the synthesis of CoNi-LDH was explained in our previous work [41]. Briefly 0.01 M of Co $(NO_3)_2$•$6H_2O$ and Ni $(NO_3)_2$•$6H_2O$ were added into 50 ml of DW. This was followed by thorough stirring for 30 minutes. This uniform solution was branded as S2. The materials were then grown directly onto the NF substrate in accordance with the procedure already described in section 2.3. With the exception that RE, WE and CE were immersed in the solution S2 instead. The resulting electrode was branded as CoNi-LDH. The same process was replicated, but now with $MnCr_2O_4$-1.2 V as the WE. The final electrode was labelled as $MnCr_2O_4$-1.2 V@CoNi-LDH. The schematic illustration in scheme 1 shows the synthesis of $MnCr_2O_4$-1.2 V@CoNi-LDH. The synthesis of the activated carbon from amarula husk (AMH) which served as the negative electrode was discussed in detail in our prior study [45].

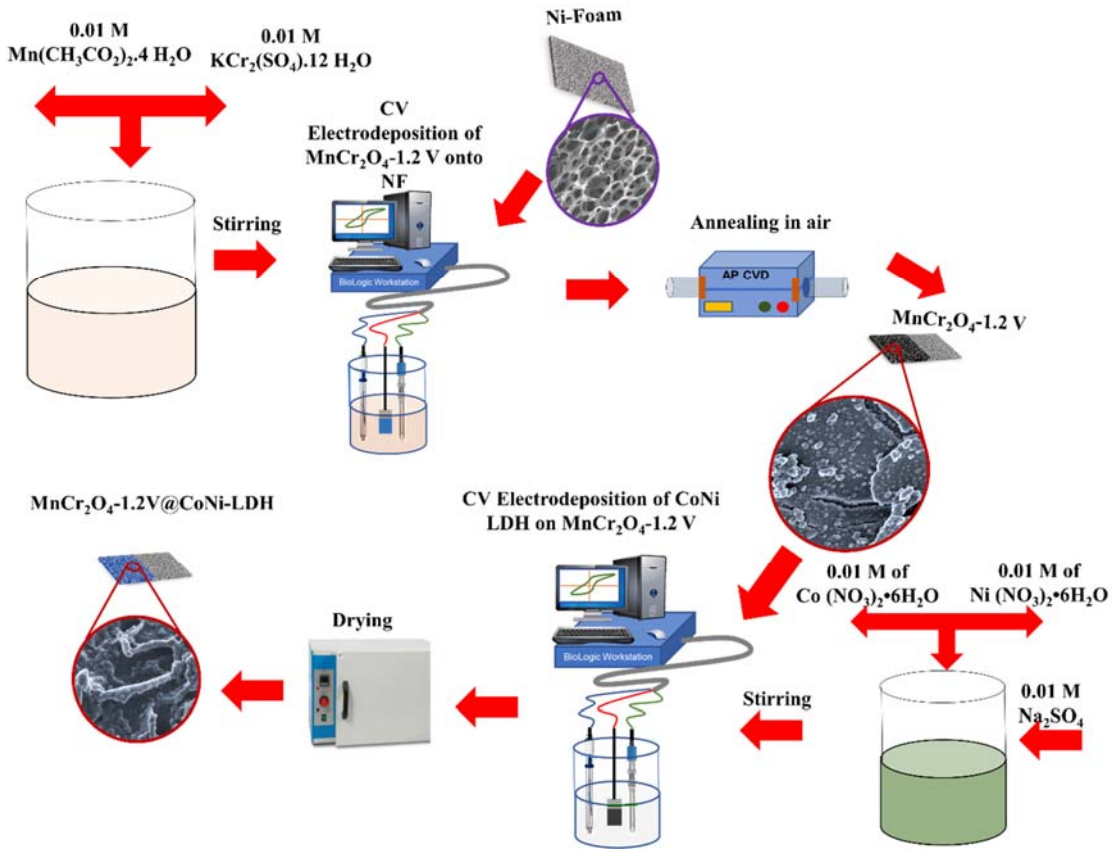

Scheme 1: Schematic illustration of the synthesis of $MnCr_2O_4$-1.2 V@CoNi-LDH electrode.

2.5 Material characterisation

To evaluate the scanning electron microscopy (SEM) morphology, elemental composition, and thickness of the $MnCr_2O_4$-ϕ, CoNi-LDH and $MnCr_2O_4$-1.2 V@CoNi-LDH electrodes, the Zeiss Ultra PLUS FEG-SEM (Ashikima-Shi, Japan) was used. This device also includes the energy dissipation spectroscopy (EDS) worked with an accelerating voltage of 2.0 kV. To obtain the transmission electron microscopy (TEM) micrograms, the JEOL JEM 2100-F device with an accelerating potential of 1.0 kV was used. The structure of the electrodes was evaluated using an X-ray diffraction (XRD) diffractometer (Brucker 2D PAN analytical BV, Amsterdam,

Netherlands). This instrument makes use of Cu $K_{\alpha 1}$ (1.54061Å) with a range of $5^o \leq 2\theta \leq 90^o$. Raman spectroscopy analysis was carried out by employing the WITec alpha-300 RAS+ Confocal micro-Raman microscope (Focus Innovations, Ulm Germany) with a 532 nm laser at a power of 4.5 mW, spectral acquisition of 300s using a 20X objective with a laser power.

2.6 Electrochemical characterisation

The assessment of the electrochemical performance of the electrodes was performed using the Bio-Logic workstation potentiostat. In a half cell set-up, the RE and CE operated as stated in section 2.3 while the WE were $MnCr_2O_4$-ϕ, CoNi-LDH, and $MnCr_2O_4$-1.2 V@CoNi-LDH. GCD, CV and electrochemical impedance spectroscopy (EIS) were all performed in 2 M KOH for both the half and full-cell configuration.

3.0 Results and analysis

3.1 Microstructural characterisation and analysis

Fig. 1 shows the SEM images of $MnCr_2O_4$-ϕ. In Fig. 1(a) the nanograins are intact leaving less channels for ion transport in $MnCr_2O_4$-1.0 V. In Fig. 1(b) there is evidence of separation of the nanograin to avail pathways for ion insertion and diffusion in $MnCr_2O_4$-1.2 V. With the increase of the electrodeposition voltage to -1.4 V, as seen in Fig. 1(c) for $MnCr_2O_4$-1.4 V the nanograins gets more separated from each other. The morphology in Fig. 1(b) appears to be the most appropriate for mobility of ions from the electrolyte, therefore, $MnCr_2O_4$-1.2 V was used to make a composite electrode material.

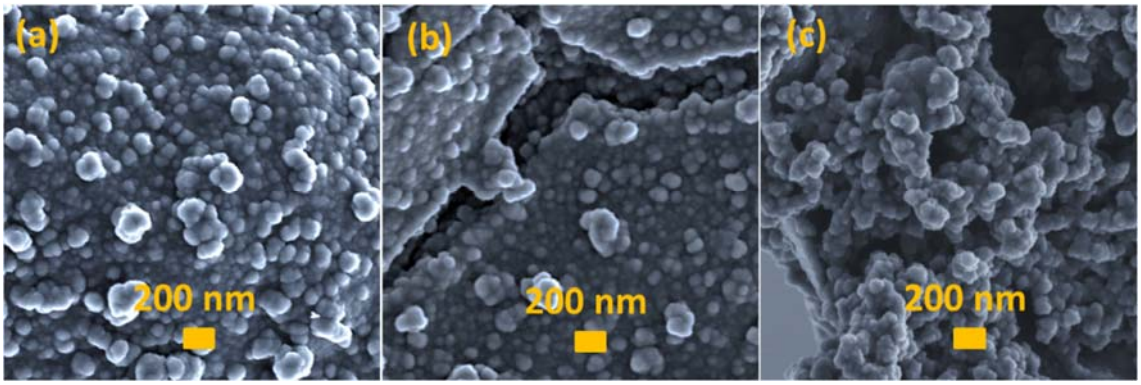

Fig. 1: SEM images of $MnCr_2O_4$-1.0 V, $MnCr_2O_4$-1.2 V and $MnCr_2O_4$-1.4 V.

Fig. 2 shows the SEM micrograms of the $MnCr_2O_4$-1.2 V, CoNi-LDH and $MnCr_2O_4$-1.2 V@CoNi-LDH electrodes. Fig. 2(a) and (b) illustrates the nanograins of $MnCr_2O_4$-1.2 V at low and high resolution, respectively. The nanograins array reveal channels which could be pathways for ion diffusion Fig. 2(c) and (d) shows the nanoflakes of CoNi-LDH at low and high magnification, respectively. The sheet like structure which is synonymous with layered material exposes open structures which could act as the electroactive sites which could lead to improvement of the electrochemical performance. Fig. 2(e) and (f) show the $MnCr_2O_4$-1.2 V@CoNi-LDH nanograins fused into a wide rolled sheet-like structure. This arrangement combines the pathways from the gaps among the nanograins and the sheet-like arrangement provides even more pathways for ion transport.

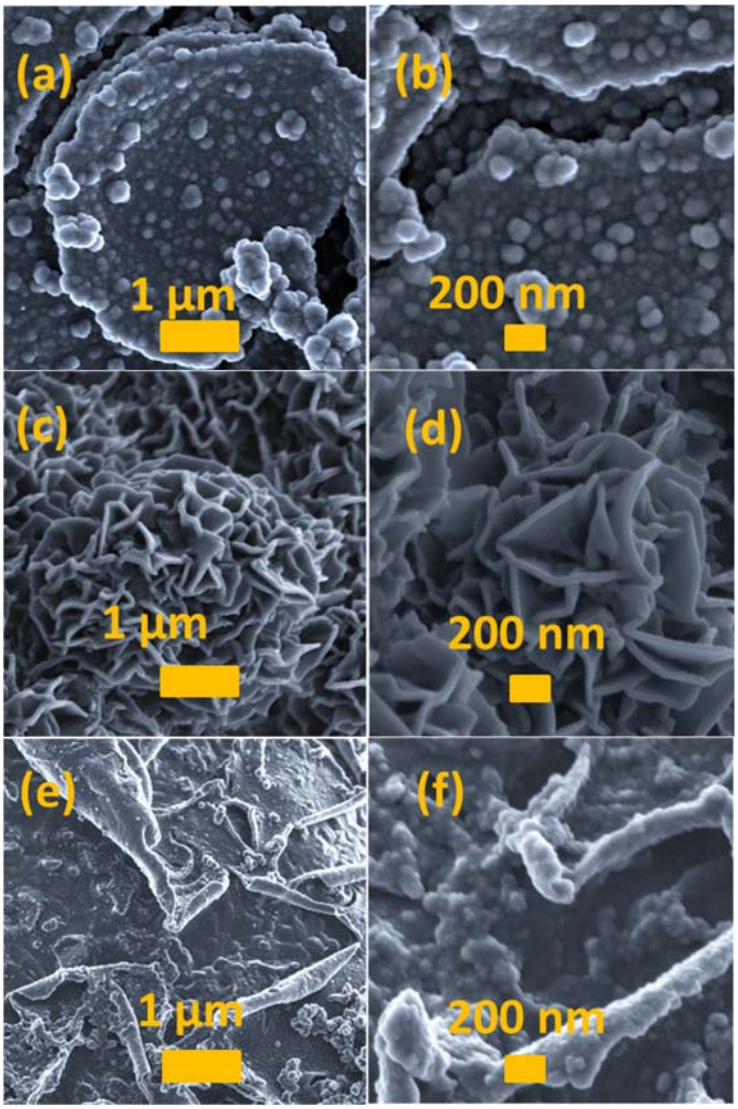

Fig. 2: (a, b), (c, d) and **(e, f)** presents low- and high-resolution micrographs of $MnCr_2O_4$-1.2 V, CoNi-LDH and $MnCr_2O_4$ -1.2 V@CoNi-LDH, respectively.

Fig. 3(a) – (f) reveals the EDS mapping of $MnCr_2O_4$-1.2V@CoNi-LDH composite signifying the homogeneous composition of the elements nickel (Ni), oxygen (O), cobalt (Co), chromium (Cr), and manganese (Mn). Fig. 3(g) indicates the percentage of these elements composition which are 64.4, 11.4, 7.7, 10.4 and 6.2 %, respectively.

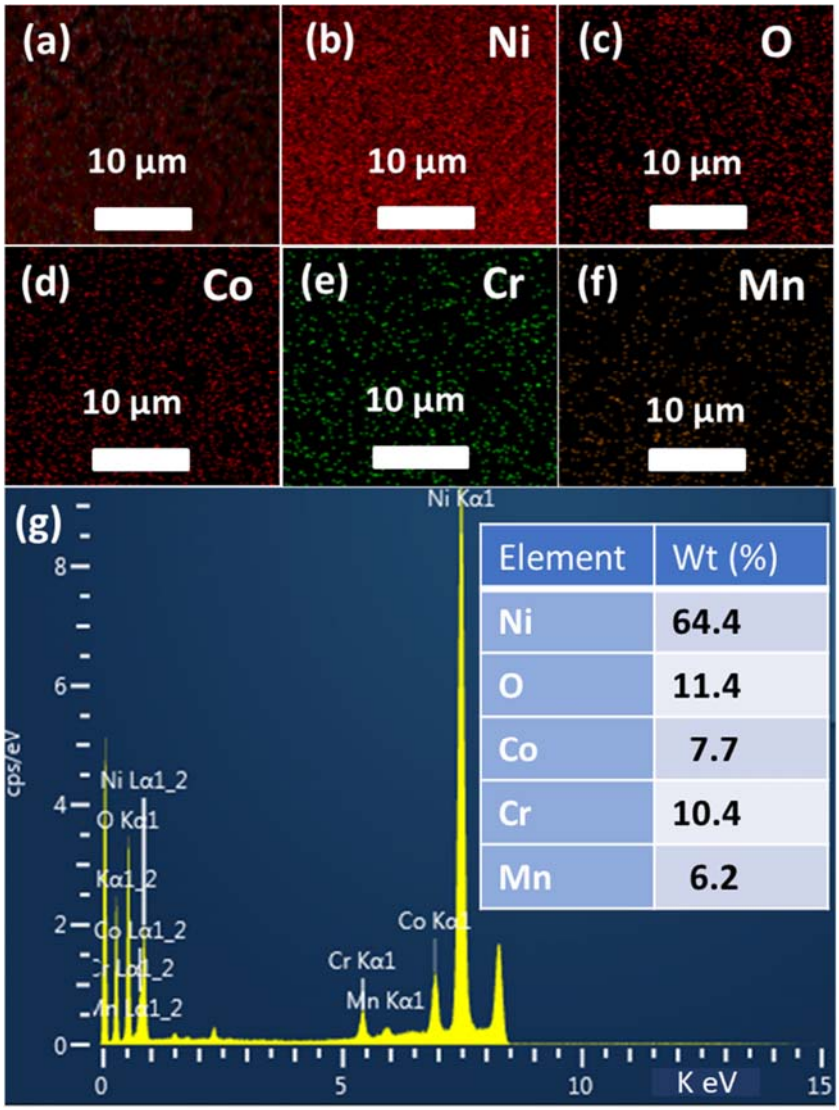

Fig. 3: (a) - (f) presents the elemental mapping of $MnCr_2O_4$-1.2V@CoNi-LDH composite sample displaying the distribution of nickel, oxygen, cobalt, chromium, and manganese, respectively and **(g)** the percentage composition of the elements within the material.

Fig. 4 (a) shows the Raman spectroscopy of $MnCr_2O_4$-1.2 V, CoNi-LDH and $MnCr_2O_4$-1.2 V@CoNi-LDH. For the $MnCr_2O_4$-1.2 V electrode, the A_{1g} peak at 794 cm^{-1} signify the presence of CrO_6 whereas the F_{2g} at 562 cm^{-1} is due to the tetrahedral cations [46]. For CoNi-LDH, the occurrence of the O-Ni-O and O-Co-O bonds is shown by the E_{1g} peak at 480 cm^{-1}

while the Co-OH and Ni-OH bonds at 673 and 545 cm^{-1} respectively are due to the A_{1g} and F_{2g} peaks, respectively. The presence of the E_{2g}, F_{2g} and two A_{1g} peaks in the $MnCr_2O_4$-1.2 V@CoNi-LDH composite electrode is evidence for the successful combination of the two individual materials to make a composite. The trivial peak shift and increase in broadness for the composite material is due to phonon confinement owing to the change in particle size [47]. Fig. 3(b) shows the XRD of $MnCr_2O_4$-1.2 V, CoNi-LDH and $MnCr_2O_4$-1.2 V@CoNi-LDH. The peaks at 18.6, 30.3, 35.6, 38.0,42.5 and 57.0° correspond to the (111), (220), (311), (400), (331) and (440) planes revealing the cubic nature of $MnCr_2O_4$ (JCPDS= 01-075-1614) [18]. The diffraction peaks occurring at a $2\theta = 9.7$, 19.4, 33.3, 38.2, 47.7, 58.7 and 61.9°, respectively correspond to the planes (003), (006), (009), (015), (018), (110) and (113) of CoNi-LDH (JCPDS No.14-0191) [48]. The appearance of these planes in $MnCr_2O_4$-1.2 V@CoNi-LDH confirms the successful synthesis of the composite from the LDH and BMO.

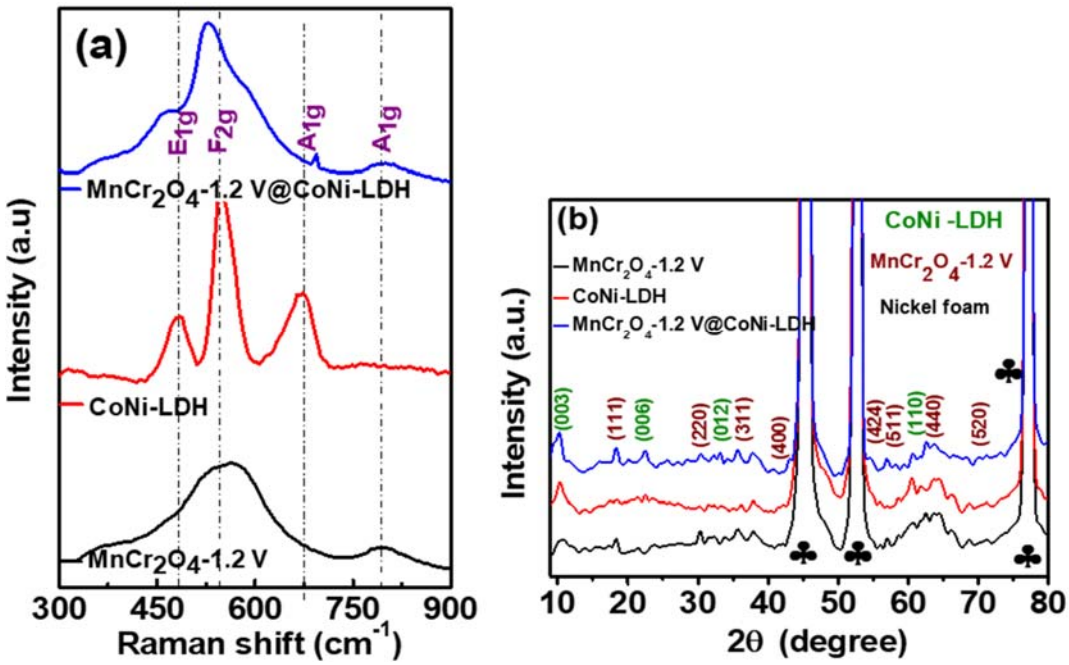

Fig. 4: (a) Raman spectrum and (b) XRD of $MnCr_2O_4$-1.2 V, CoNi-LDH and $MnCr_2O_4$-1.2 V@CoNi-LDH.

3.2 Electrochemical performance of the as-synthesized samples

3.2.1 Three-electrode evaluations

Fig. 5 (a) displays the GCD of $MnCr_2O_4$-1.2V in various electrolytes at 1 A g^{-1}. 2 M KOH gives the largest discharge time compared to other neutral and alkaline electrolytes. Fig. 5(b) shows the CV of $MnCr_2O_4$-1.0 V, $MnCr_2O_4$-1.2V, $MnCr_2O_4$-1.4V and Nickel foam in 2 M KOH electrolyte at 20 mV s^{-1}. $MnCr_2O_4$-1.2V shows the greatest current response compared to the other electrodes. The trace for nickel foam is barely visible leading to the conclusion that its contribution to the electrochemical performance of the active materials is negligible. Fig. 5(c) shows the GCD of $MnCr_2O_4$-1.0 V, $MnCr_2O_4$-1.2 V and $MnCr_2O_4$-1.4 V at 1 A g^{-1} in 2 M KOH. All the discharge curves are characterised by nonlinear discharges signifying the accumulation of charges due to Faradaic redox reaction. The $MnCr_2O_4$-1.2 V electrode gives the most extended discharge time signifying the highest specific capacity. Fig. 5 (d) shows the specific capacity for these three electrodes. Equation 1 was used to calculate the specific capacity (Q_S) [49].

$$Q_S\ [C\ g^{-1}] = I_S \Delta t \qquad (1)$$

where I_S is the specific current (A g^{-1}) and Δt is the discharge time (s). The specific capacities are 180.1, 557.3 and 347.3 C g^{-1}. This shows that the electrodeposition voltage of -1.2 V using the scan rate of 2.5 mV s^{-1} yields the best electrochemical performance for the electrodes. For this reason, $MnCr_2O_4$-1.2 V was used for the fabrication of the composite electrode for further evaluations.

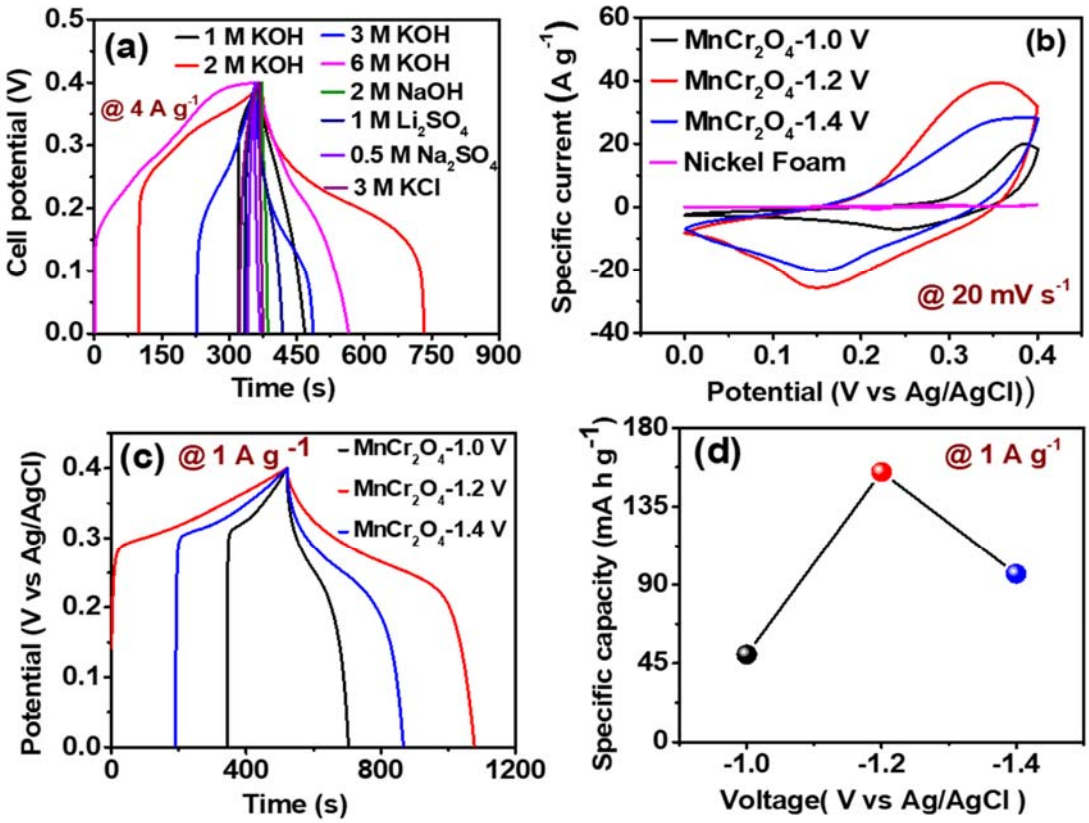

Fig 5: (a) The GCD of $MnCr_2O_4$-1.2V in various electrolytes at 1 A g^{-1}. **(b)** CV of $MnCr_2O_4$-1.0 V, $MnCr_2O_4$-1.2V, $MnCr_2O_4$-1.4V and Nickel foam in 2 M KOH electrolyte at 20 mV s^{-1}. **(c)** The GCD of $MnCr_2O_4$-1.0 V, $MnCr_2O_4$-1.2V, $MnCr_2O_4$-1.4V at 1 A g^{-1} **(d)** Specific capacity vs electrodeposition voltage of $MnCr_2O_4$-1.0 V, $MnCr_2O_4$-1.2V and $MnCr_2O_4$-1.4V in 2 M KOH electrolyte.

Fig. 6 shows the comparison of the electrochemical performance of $MnCr_2O_4$-1.2 V, CoNi-LDH and $MnCr_2O_4$-1.2 V@CoNi-LDH in a half cell set-up in 2 M KOH. Fig. 6(a) shows the CV in a voltage range 0 – 0.4 V vs Ag/AgCl. All the electrodes show peaks which emanate from Faradaic reactions. The composite electrode, $MnCr_2O_4$-1.2 V@CoNi-LDH has the largest current response in this voltage range. This Faradaic charge storage mechanism is also confirmed by the GCD in Fig. 6(b) with the plateaux signify the accumulation of charges. The longest discharge time in the $MnCr_2O_4$-1.2 V@CoNi-LDH can be explained by the abundant

exposed redox active sites in CoNi-LDH. Fig. 6(c) shows the specific capacity of the electrodes for a range of specific current of 1 - 10 A g^{-1}.

The specific capacities are 557.3, 1170.3 and 1529.3 C g^{-1} for $MnCr_2O_4$-1.2 V, CoNi-LDH and $MnCr_2O_4$-1.2 V@CoNi-LDH, respectively. $MnCr_2O_4$-1.2 V@CoNi-LDH also shows the highest rate capability at 10 A g^{-1}. The rate capabilities values are 42.3, 54.3 and 59.4 %, respectively. Fig. 6(d) shows the EIS Nyquist plot of the electrodes with the inset showing the enlarged high frequency region exposing the equivalent series resistance (ESR) of electrode. The equivalent series resistance (ESR) values as read from the intercept with x-axis are 1.9, 1.3 and 1.6 Ω for $MnCr_2O_4$-1.2 V, CoNi-LDH and $MnCr_2O_4$-1.2 V@CoNi-LDH respectively. These low ESR values are credited to the intact bonding of the electrode materials and the NF current collector due to the electrodeposition synthesis which also excludes polymeric binder which would otherwise introduce some resistivity. The low magnitude of the imaginary impedance is due to the large value of the specific capacitance of the electrodes [50]. Fig. 6(e) displays the coulombic efficiency of the electrodes which is obtained using equation 2 [51].

$$\eta_C\,[\%] = \frac{t_D}{t_C} \tag{2}$$

where η_C is the coulombic efficiency, t_D and t_C are the discharging and charging times (s). The quasi-perfect coulombic efficiency values are attributed to the robustness of the electrodeposition synthesis.

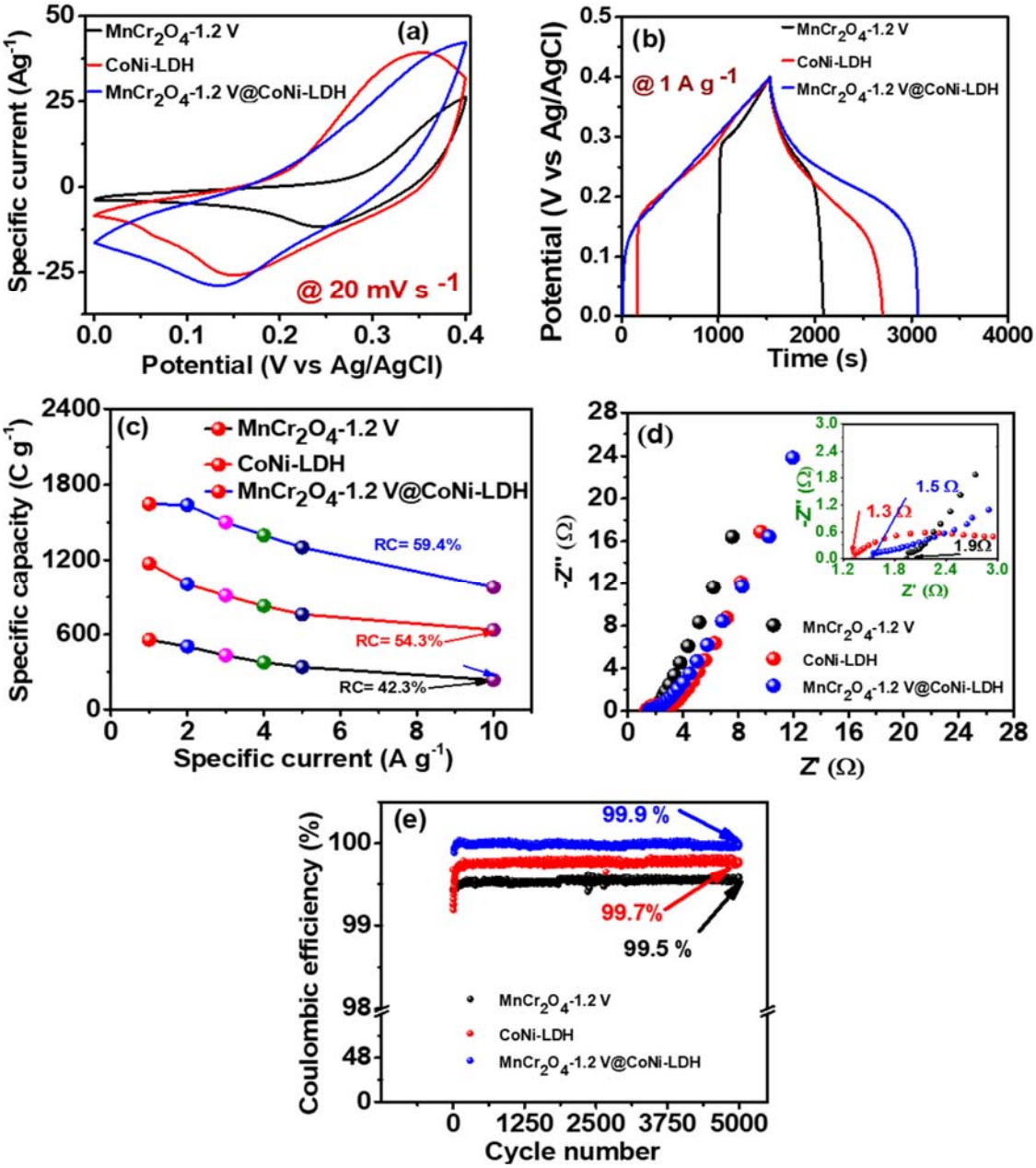

Fig. 6: Electrochemical comparison of $MnCr_2O_4$-1.2 V, CoNi-LDH and $MnCr_2O_4$-1.2 V@CoNi-LDH in 2 M KOH; (a) CV curves, (b) GCD curves, (c) specific capacity vs specific current, (d) EIS Nyquist plot and the inset to magnify the high frequency region and (f) coulombic efficiency.

Fig. 6(e) show the coulombic efficiency of the electrodes as a function of number of cycles, the large value of the coulombic efficiency (99.5, 99.7 and 99.9 %, respectively) are partially credited to the mechanical stability of the synthesis method. The largest value of $MnCr_2O_4$-1.2 V@CoNi-LDH shows the stability introduced by the LDH and the BMO.

Due to the superiority shown by $MnCr_2O_4$-1.2 V@CoNi-LDH in the electrochemical comparison in Fig. (6), it was opted for further analysis for use as a positive electrode in a device using the same electrolyte (2 M KOH). The electrochemical performance of $MnCr_2O_4$-1.2 V@CoNi-LDH in 2 M KOH in a half-cell configuration are shown in Fig. 7. Fig. 7(a) display the CV in a voltage rage from 0 - 0.4 V vs Ag/AgCl. The increase with current due to the Randles-Sevcik equation, which states that the peak current (i_p) is proportional to the square-root of the scan-rate, ν such that $i_p \propto \sqrt{\nu}$ [52]. Oxidation peaks become less pronounced in the voltage range as the scan rate increases. This is because at low scan rate the electrolyte ions and the electrode's active species have ample time to interact with each other increasing the likelihood of redox reactions. As the scan rate increases, the interaction time decrease so the reactions between the electrode species and the ions are suppressed [53]. In the GCD in Fig. 7(b), the plateaux further support the notion of Faradaic reactions. The decrease of charging and discharging time with a rise in specific current is due to the inverse relationship between current and charge/discharge time for a fixed voltage to charge/discharge to a constant charge (I=Q/t). The stability of the composite electrode is shown by the variation of the coulombic efficiency and capacity retention with of cycle number in Fig. 7(c). The high capacity retention value of 73.6 % is caused by a combination of the two materials coupled with the mechanical strength of the electrodeposition synthesis enabling the composite electrode to retain reversibility due to the ability to overcome mechanical stress.

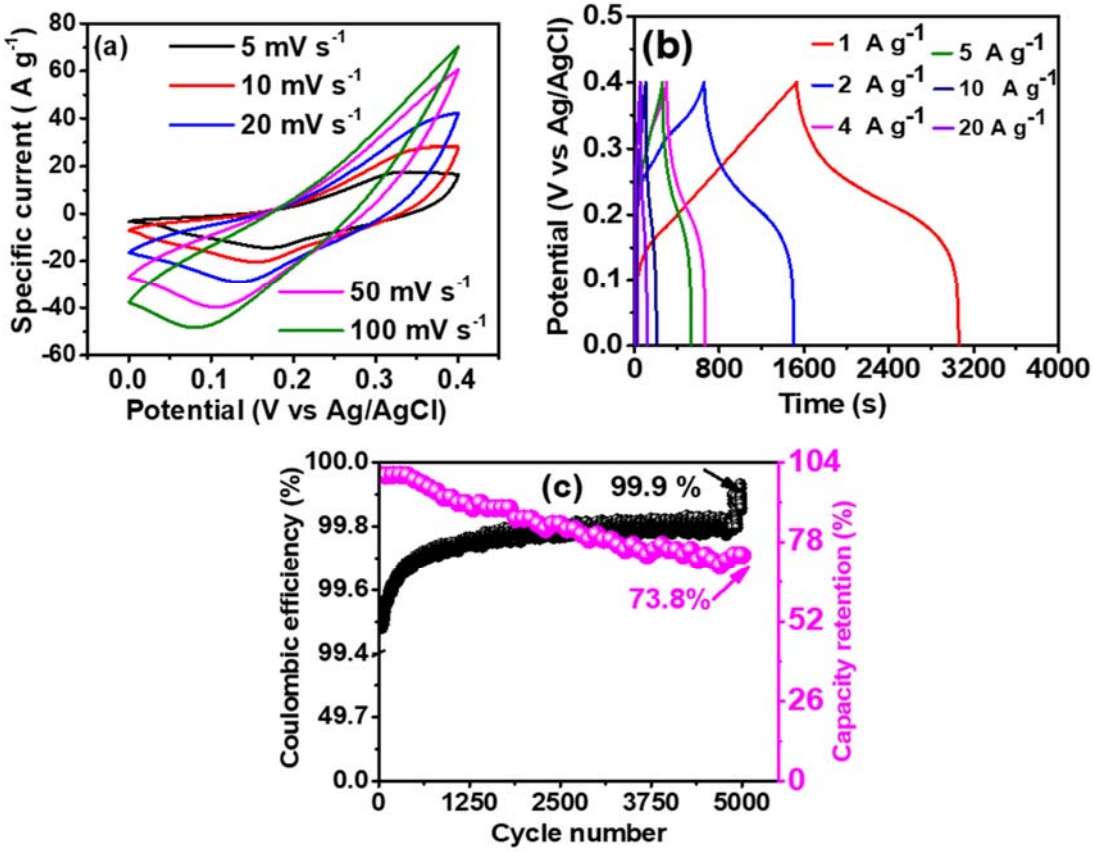

Fig. 7: (a) CV curves, (b) GCD and (c) Capacity retention and coulombic efficiency as a function of the number of cycles of $MnCr_2O_4$-1.2 V@CoNi-LDH.

Table 1 contrasts the electrochemical performance of chrome based supercapacitor electrodes. It is transparent from the table that the electrode synthesised in this work using electrodeposition and annealing produced comparable stability and superior specific capacity in three-electrode set-up. This makes it appropriate for participating in supercapacitor devices.

Table 1: Electrochemical performance of newly reported chromium-based composites in three-electrode system.

Electrode	Synthesis method	Capacity retention (%)	Cycle number	Specific capacity ($C\ g^{-1}$)	Specific current ($A\ g^{-1}$)	Reference:
(NG)/$CuCr_2O_4$	Mechanical mixing	98.3	5,000	66.2	0.5	[50]
NG/$CuCr_2O_4$/PANI	Mechanical mixing	92	10,000	199.4	1	[54]
CP-CR	Polymerization	77	5,000	263.5	1	[55]
$La(CoCrFeMnNiAl_{0.5})_{1/5}$ $.5O_{3-\delta}$	Coprecipitation and calcination	88.6	2,000	176.4	1	[56]
$Mn^{II}Cr^{III}_2O_4/Mn^{II}Mn^{III}_2O_4$/ C	Annealing	75.2	5,000	662.4	0.5	[57]
$MgCr_2O_4$	Sol-gel	84	1,000	20.9	0.25	[58]
$MnCr_2O_4$	Electrodeposition	78	1,000	910.8	0.1	[18]
MIL-101(Cr)	Hydrothermal	86	85	117.7	1	[59]
Cr_2O_3	Sol-gel	85	85	254.9	0.5	[60]
Ni_2Cr_1-LDNs	Mechanical mixing	80	10,000	608.4	2	[61]
FGO-Ap/Cr	Hydrothermal	96.9	5,000	370.8	1	[62]
$MnCr_2O_4$-1.2V @CoNi-LDH	Electrodeposition and annealing	73.6	5,000	1528.9	1	**This work**

3.2.2 Electrochemical properties of the hybrid supercapacitor device

To assess the compatibility of $MnCr_2O_4$-1.2 V@CoNi-LDH as a positive electrode in a supercapacitor device, an asymmetric devices $MnCr_2O_4$-1.2 V@CoNi-LDH//AMH, where AMH served as the negative electrode was fabricated. The analysis was performed in a 2-electrode set-up in 2 M KOH electrolyte. To ensure the maximum efficiency of the device, it is essential to perform a mass balance of the electrodes using equation 3 [63,64].

$$\frac{m_+}{m_-} = \frac{C_{S-} \times V_{S_-}}{Q_{S+}} \tag{3}$$

where $m_+/m\_\_$ is the ratio of the masses of the positive to the negative electrode, C_{S-} is the specific capacitance (F g^{-1}), V_{S-} is the negative electrode potential (V) and Q_{S+} is the specific capacity (C g^{-1}). The mass of the negative and positive electrodes used for the devices on each electrode were 5.0 and 0.75 mg cm^{-2}, respectively equivalent to a mass ratio $m_+ : m\_\_$ of 20:3. The total mass of the electrode per unit area was 5.75 mg cm^{-2}.

Fig. 8(a) shows the CV curves of the negative and positive electrodes in three-electrodes configuration. The CV of AMH (negative electrode) in a voltage range of -0.8 - 0 V vs Ag/AgCl shows a quasi-rectangular trace and peaks which is evidence for non-Faradaic energy storage mechanism synonymous with EDLC materials. The curve of $MnCr_2O_4$-1.2 V@CoNi-LDH in a voltage range of 0 - 0.4 V vs Ag/AgCl shows a pair of redox peaks revealing Faradaic redox reaction based energy storage mechanism. Fig. 8(b) illustrates the CV curves of the device in a voltage range of 0 - 1.6 V with scan rates of 5 - 100 mV s^{-1}. In the potential range of 0 - 0.8 V the capacitive behaviour of AMH is dominant without any peaks. From voltage of 0.8 - 1.6 V, there is a sharp increase in current response due to the accumulation of charge due to the manifestation of redox reactions from $MnCr_2O_4$-1.2 V@CoNi-LDH. The GCD in Fig. 8(c) confirms the presence of both Faradaic and EDLC behaviour where the slanted plateaux are visible from the potential range of 1.6 - 0.8 V and quasi-linear discharge is shown from 0.8 - 0

V. The symmetry of curves for the specific current range of 0.5 - 10 A g^{-1} is due to the reversibility of the charge storage processes [62]. Fig. 8(d) shows the variation of the specific capacity with specific current. The highest specific capacity is 257.9 C g^{-1} at a specific current of 1 A g^{-1}, while the specific capacity at 20 A g^{-1} is 130.9 C g^{-1} corresponding to a rate capability of 50.7 %. Fig. 8(e) displays the capacity retention and coulombic efficiency as a function of number of cycles. The capacity retention and coulombic efficiency values are 72.9 and 99.7 %, respectively after 15,000 GCD cycles at 9 A g^{-1}. The inherent high stability of AMH and the synergetic effect of CoNi-LDH and $MnCr_2O_4$-1.2V contributed to these phenomenal stability values. The specific energy (E_S) and power (P_S) were calculated using equations 4 and 5 [65,66].

$$E_S\ [Wh\ kg^{-1}] = \frac{I_S}{3.6} \times \int V dt \tag{4}$$

$$P_S\ [W\ kg^{-1}] = \frac{3600}{\Delta t} \times E_S \tag{5}$$

where I_S is the specific current (A g^{-1}), $\int V dt$ is the area (integral) under the discharge curve (Vs) and Δt is the discharge time (s). E_S for the device was 80.2 Wh kg^{-1} corresponding to P_S of 1117.7 W kg^{-1}. Fig. 8(f) presents the Ragone plot to show the comparison of this hybrid device with related chromium based supercapacitor devices in the literature according to the specific power and specific energy [55,58,67–70]. The insert shows a circuit with 4 diodes connected in parallel lighted by the hybrid device. This plot clearly shows that this work produced a very competitive device with great energy and power output. The circuit demonstrates the practical applicability of the energy delivery.

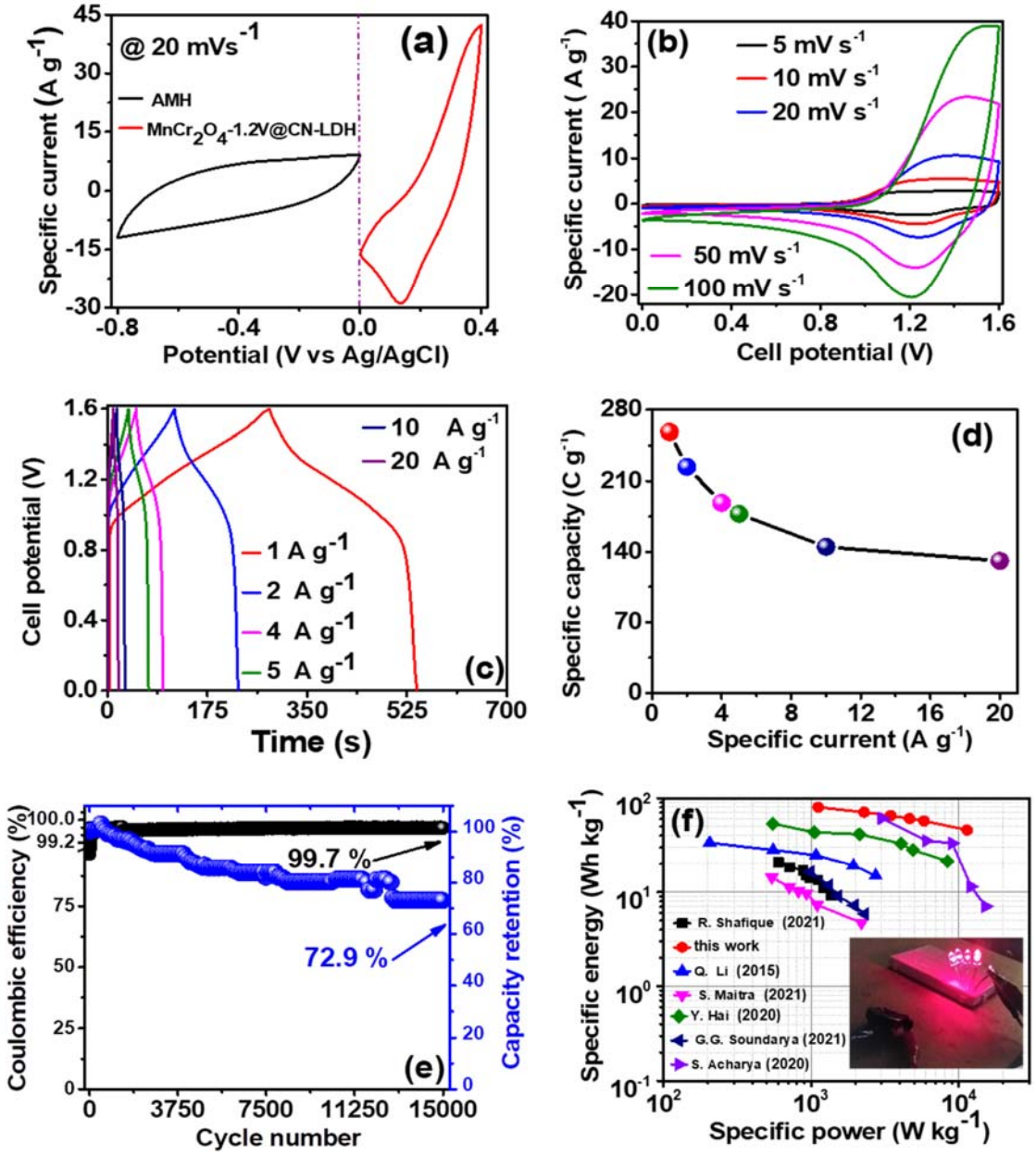

Fig. 8 (a) CV traces of the negative electrode (AMH), and positive electrodes ($MnCr_2O_4$-1.2 V@CoNi-LDH) at 20 mV s^{-1}, b) CV curves at different scan rates, (c) GCD curves at various specific currents, (d) the specific capacity as a function of specific current, (e) capacity retention and coulombic efficiency vs cycle number and (f) Ragone plot of $MnCr_2O_4$-1.2 V@CoNi-LDH//AMH hybrid device compared to other related devices in the literature, the insert shows 4 diodes in parallel lighted by this hybrid device.

Fig. 9(a) shows the Nyquist plot of the EIS experimental data from the device together with the fitting. The insert shows the equivalent circuit used to perform the fitting. The equivalent series resistance (R_S) in the circuit is linked with to the real impedance intercept of the plot at high frequency. The source of this resistance is the opposition to the flow of charges at the electrode/electrolyte intersection and between the electrode and the current collector [71]. (R_S) is in series with the charge transfer resistance (CTR), the constant phase element (CPE), and the Warburg element (W) represented by circuit elements; R_{CT}, Q and Z_W, respectively. CTR is due to the presence of Faradaic reactions depicted by a small semi-circle in the mid-frequency region [72]. The semi-circle is suppressed due to the presence of the CPE which emanate from non-ideal capacitance due to microscopic roughness caused by scratching at the surface of the electrode [73]. CPE is in series with W. W represents the diffusion through the electrode material [74]. It is responsible for the divergence of the line away from the imaginary impedance axis at the low frequency. These elements are in turn in series with a parallel branch containing the double layer capacitance and the leakage current resistance represented by the circuit elements C_{DL} and R_L, respectively. Ideal C_{DL} behaviour causes the plot to be parallel to the imaginary impedance axes. R_L is the opposition to the movement of ions as they try to reach deep inside fine pores of porous material [75]. Fig. 9(b) indicates the comparison of the Nyquist plot before and after running stability using 15,000 GCD cycles. R_S decreases slightly from 1.54 to 1.46 Ω after stability due to the decrease in the resistance at the electrode/electrolyte and the electrode/ current collector interfaces. There is a very small increase in the imaginary impedance at the low frequency region after cycling, the is caused by rise in the diffusion length on the electrode/electrolyte interface due to the decomposition of water molecules in the aqueous electrolyte [76].

R_S can be used to calculate the maximum power from the device to the load. This maximum power, according to the maximum power transfer theorem is transferred when the resistance of the load and R_S are equal. It is calculated from equation 6 [77].

$$P_{MAX}\ [kW\ kg^{-1}] = \frac{V^2}{4mR_S} \tag{6}$$

where V is the cell potential (V), m is the total mass of the electrode material (g) and R_S is the solution resistance (Ω). The P_{MAX} for the device is 111 kW kg^{-1}.

Fig. 9(c) represents the Bode plot indicating the phase angle variation with frequency. The maximum phase angle of -72^o which isn't far from the ideal -90^o for ideal capacitive behaviour due to the presence of AMH which is an EDLC material. Fig. 9(d) demonstrates the real and imaginary capacitances ($C'\ and\ C''$) respectively as a function of frequency (f). $C'\ and\ C''$ are calculated from equation (5) and (6), respectively [78].

$$C'(\omega)[F] = -\frac{Z''(\omega)}{\omega|Z\ (\omega)|^2} \tag{7}$$

$$C''(\omega)[F] = -\frac{Z'(\omega)}{\omega|Z\ (\omega)|^2} \tag{8}$$

where $Z''(\omega), Z'(\omega)$ and $|Z\ (\omega)|$ are the imaginary impedance, real impedance, and magnitude of the impedance (Ω), respectively, and $\omega = 2\pi f$ is the angular frequency (rad s^{-1}).

(C') relates to the useful energy that can be transferred and (C'') is due to the unrecovered energy due to irreversible processes. The peak of the C'' is 221 mF occurring at a frequency of 41 mHz corresponding to a relaxation time (τ) of 3.9 s while the peak of $C'$is 277 mF. This low τ value signify the ability of the device to be charged quicky. It is obtained from $\omega\tau = 1$ [79].

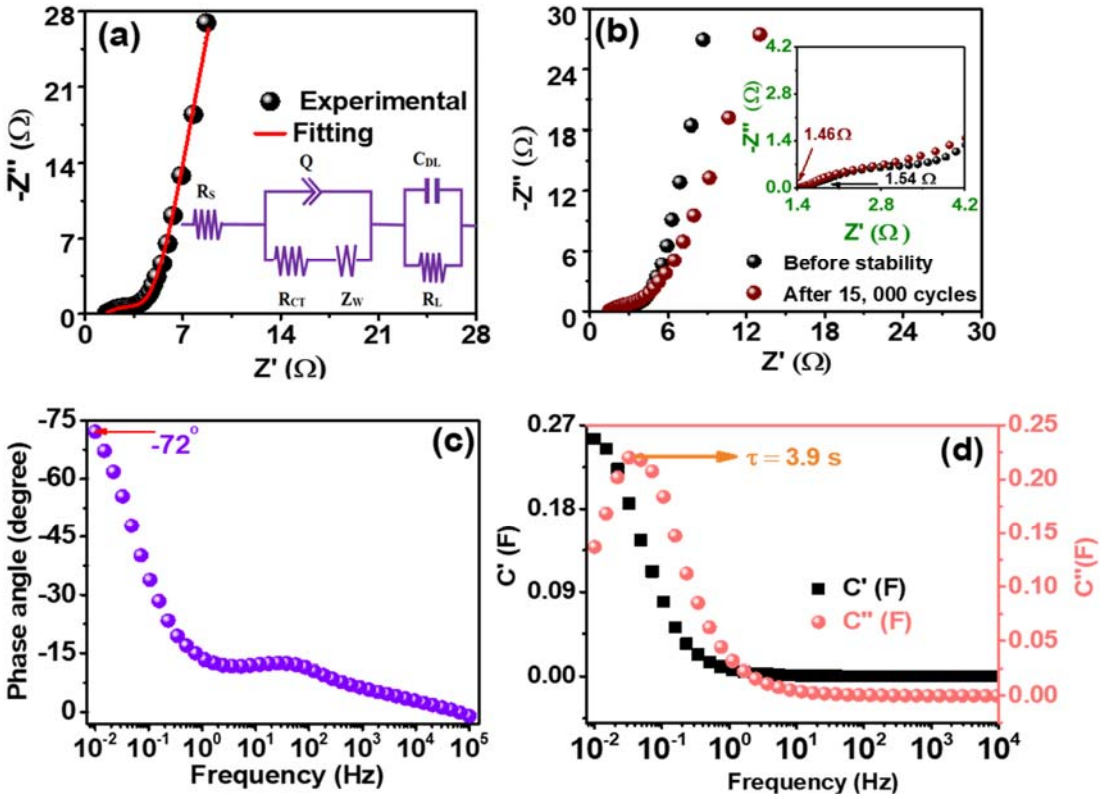

Fig. 9: (a) Nyquist plot for the experimental data and the fitting curve of the equivalent circuit as the inset, (b) Nyquist plot before and after 15, 000 GCD cycles with inset being the enlargement of the higher frequency region, (c) Bode plot and (d) Real and imaginary capacitance vs frequency of the device.

4.0 Conclusion

$MnCr_2O_4 - \phi$, was electrodeposited onto NF. This was done by varying ϕ, the CV electrodeposition potentials (V) to, -1.4, -1.2 and -1.0 V to obtain three electrodes which were then annealed. Of these electrodes, $MnCr_2O_4$-1.2 V electrode produced the best electrochemical results and was selected for the synthesis of the composite electrode $MnCr_2O_4$-

1.2V @CoNi-LDH. This was achieved by performing a second electrodeposition of CoNi-LDH on $MnCr_2O_4$-1.2V.

The structural, morphological, and elemental analysis reveals the successively formation of the composite electrode material. The electrode yielded excellent electrochemical performance in 2 M KOH in a three-electrode with a specific capacity of 1529.3 C g^{-1} at a of 1 A g^{-1}. The electrode was incorporated into an asymmetric supercapacitor device ($MnCr_2O_4$-1.2V @CoNi-LDH//AMH) with AMH as the negative electrode. The device also produced exceptional results with a huge specific capacity of 257.9 C g^{-1} at 1 A g^{-1}. The specific energy of the device was 80.2 W h kg^{-1} at 1 A g^{-1} relating to a specific power of 1117 W kg. The device also showed the capacity retention and Coulombic efficiency of the device were 72.9 and 99.7%, respectively after 15 000 GCD cycles at 9 A g^{-1}This phenomenal performance avails the produced hybrid device as a contender for high energy and power applications.

Acknowledgements

This research was facilitated by the South African Research Chairs Initiative (SARChI) of the Department of Science and technology and the National Research foundation (NRF) South Africa (Grant number. 61056). All the ideas, findings, recommendations, and conclusions in this work are from of author(s) therefore NRF does not take any liability in this regard. Gift Rutavi recognises the support from NRF through SARChI in Carbon materials.

References

[1] M. Moniruzzaman, Y. Anil Kumar, M.R. Pallavolu, H.M. Arbi, S. Alzahmi, I.M. Obaidat, Two-Dimensional Core-Shell Structure of Cobalt-Doped@MnO2 Nanosheets Grown on Nickel Foam as a Binder-Free Battery-Type Electrode for Supercapacitor Application, Nanomaterials. 12 (2022). https://doi.org/10.3390/nano12183187.

[2] C. Yang, L. Hong, P. Chong, Y. Li, M. Wei, Tin-based metal-phosphine complexes nanoparticles as long-cycle life electrodes for high-performance hybrid supercapacitors, J. Colloid Interface Sci. 606 (2022) 148–157. https://doi.org/10.1016/j.jcis.2021.08.012.

[3] Z. Sun, H. Qi, M. Chen, S. Guo, Z. Huang, S. Maganti, V. Murugadoss, M. Huang, Z. Guo, Progress in Cellulose/Carbon Nanotube Composite Flexible Electrodes for Supercapacitors, Eng. Sci. 18 (2022) 59–74. https://doi.org/10.30919/es8d588.

[4] Y. Cao, W. Yang, M. Wang, N. Wu, L. Zhang, Q. Guan, H. Guo, Metal-organic frameworks as highly efficient electrodes for long cycling stability supercapacitors, Int. J. Hydrogen Energy. 46 (2021) 18179–18206. https://doi.org/10.1016/j.ijhydene.2021.03.003.

[5] R. Liu, A. Zhou, X. Zhang, J. Mu, H. Che, Y. Wang, T.T. Wang, Z. Zhang, Z. Kou, Fundamentals, advances and challenges of transition metal compounds-based supercapacitors, Chem. Eng. J. 412 (2021) 128611. https://doi.org/10.1016/j.cej.2021.128611.

[6] S.Y. Hsu, F.H. Hsu, J.L. Chen, Y.S. Cheng, J.M. Chen, K.T. Lu, The supercapacitor electrode properties and energy storage mechanism of binary transition metal sulfide MnCo2S4compared with oxide MnCo2O4studied using: In situ quick X-ray absorption spectroscopy, Mater. Chem. Front. 5 (2021) 4937–4949.

https://doi.org/10.1039/d1qm00222h.

[7] R.M. Obodo, N.M. Shinde, U.K. Chime, S. Ezugwu, A.C. Nwanya, I. Ahmad, M. Maaza, P.M. Ejikeme, F.I. Ezema, Recent advances in metal oxide/hydroxide on three-dimensional nickel foam substrate for high performance pseudocapacitive electrodes, Curr. Opin. Electrochem. 21 (2020) 242–249. https://doi.org/10.1016/j.coelec.2020.02.022.

[8] Y. Anil Kumar, H.J. Kim, Effect of time on a hierarchical corn skeleton-like composite of CoO@ZnO as capacitive electrode material for high specific performance supercapacitors, Energies. 11 (2018). https://doi.org/10.3390/en11123285.

[9] S. Malik, I.H. Gul, M.M. Baig, Hierarchical MnNiCo ternary metal oxide/graphene nanoplatelets composites as high rated electrode material for supercapacitors, Ceram. Int. 47 (2021) 17008–17014. https://doi.org/10.1016/j.ceramint.2021.02.272.

[10] A.M. Baena-Moncada, V. Quispe-Garrido, G. Antonio Cerron-Calle, A. Bazan-Aguilar, J.G. Ruiz-Montoya, E.O. López, Advances in the design and application of transition metal oxide-based supercapacitors, Open Chem. 19 (2021) 709–725. https://doi.org/10.1515/chem-2021-0059.

[11] Y. Liu, K. Wang, X. Xu, K. Eid, A.M. Abdullah, L. Pan, Y. Yamauchi, Recent Advances in Faradic Electrochemical Deionization: System ArchitecturesversusElectrode Materials, ACS Nano. 15 (2021) 13924–13942. https://doi.org/10.1021/acsnano.1c03417.

[12] S. Kumar, G. Saeed, L. Zhu, K.N. Hui, N.H. Kim, J.H. Lee, 0D to 3D carbon-based networks combined with pseudocapacitive electrode material for high energy density supercapacitor: A review, Chem. Eng. J. 403 (2021) 126352. https://doi.org/10.1016/j.cej.2020.126352.

[13] J.H. Yoon, Y.A. Kumar, S. Sambasivam, S.A. Hira, T.N.V. Krishna, K. Zeb, W. Uddine, K.D. Kumar, I.M. Obaidat, S. Kim, H.J. Kim, Highly efficient copper-cobalt sulfide nano-reeds array with simplistic fabrication strategy for battery-type supercapacitors, J. Energy Storage. 32 (2020) 101988. https://doi.org/10.1016/j.est.2020.101988.

[14] D. Mohanadas, Y. Sulaiman, Recent advances in development of electroactive composite materials for electrochromic and supercapacitor applications, J. Power Sources. 523 (2022) 231029. https://doi.org/10.1016/j.jpowsour.2022.231029.

[15] X. Zhao, L. Mao, Q. Cheng, J. Li, F. Liao, G. Yang, L. Xie, C. Zhao, L. Chen, Two-dimensional Spinel Structured Co-based Materials for High Performance Supercapacitors: A Critical Review, Chem. Eng. J. 387 (2020) 124081. https://doi.org/10.1016/j.cej.2020.124081.

[16] J.G. Ruiz-Montoya, Lady V. Quispe-Garrido, J.C. Calderón Gómez, A.M. Baena-Moncada, J.M. Goncąlves, Recent progress in and prospects for supercapacitor materials based on metal oxide or hydroxide/biomass-derived carbon composites, Sustain. Energy Fuels. 5 (2021) 5332–5365. https://doi.org/10.1039/d1se01170g.

[17] Y. Li, S. Feng, Q. Lv, X. Kan, X. Liu, An investigation of reentrant spin-glass behavior, magnetocaloric effect and critical behavior of MnCr2O4, J. Alloys Compd. 877 (2021) 160224. https://doi.org/10.1016/j.jallcom.2021.160224.

[18] F.F. Alharbi, S. Aman, N. Ahmad, S.R. Ejaz, S. Manzoor, R.Y. Khosa, M.U. Nisa, M.A. Iqbal, S. Abbas, M. Awais, Design and fabrication of novel MnCr2O4 nanostructure: electrochemically deposited on stainless steel strip with enhanced efficiency towards supercapacitor applications, J. Mater. Sci. Mater. Electron. 33 (2022) 7256–7265. https://doi.org/10.1007/s10854-022-07909-3.

[19] M. Gul, Radio frequency abnormal dielectric response of manganese chromite (MnCr2O4) nanoparticles synthesized by coprecipitation method, Mater. Res. Bull. 76 (2016) 431–435. https://doi.org/10.1016/j.materresbull.2016.01.007.

[20] P.R. Kharangarh, N.M. Ravindra, R. Rawal, A. Singh, V. Gupta, Graphene quantum dots decorated on spinel nickel cobaltite nanocomposites for boosting supercapacitor electrode material performance, J. Alloys Compd. 876 (2021) 159990. https://doi.org/10.1016/j.jallcom.2021.159990.

[21] R. Ramachandran, Y. Lan, Z.X. Xu, F. Wang, Construction of NiCo-Layered Double Hydroxide Microspheres from Ni-MOFs for High-Performance Asymmetric Supercapacitors, ACS Appl. Energy Mater. 3 (2020) 6633–6643. https://doi.org/10.1021/acsaem.0c00790.

[22] Y. Zhu, S. An, X. Sun, D. Lan, J. Cui, Y. Zhang, W. He, Core-branched NiCo2S4@CoNi-LDH heterostructure as advanced electrode with superior energy storage performance, Chem. Eng. J. 383 (2020) 123206. https://doi.org/10.1016/j.cej.2019.123206.

[23] X. Zhang, Q. Lu, E. Guo, J. Feng, M. Wei, J. Ma, NiCo layer double hydroxide/biomass-derived interconnected porous carbon for hybrid supercapacitors, J. Energy Storage. 38 (2021) 102514. https://doi.org/10.1016/j.est.2021.102514.

[24] W. Zhou, X. Yan, W. Zhang, Y. Li, Y. Zhu, M. Zhang, W. Zhu, X. Cheng, Tailored synthesis of nano-corals nickel-vanadium layered double hydroxide@Co2NiO4 on nickel foam for a novel hybrid supercapacitor, J. Energy Storage. 38 (2021) 102584. https://doi.org/10.1016/j.est.2021.102584.

[25] H. Liang, T. Lin, S. Wang, H. Jia, C. Li, J. Cao, J. Feng, W. Fei, J. Qi, A free-standing manganese cobalt sulfide@cobalt nickel layered double hydroxide core-shell

heterostructure for an asymmetric supercapacitor, Dalt. Trans. 49 (2019) 196–202. https://doi.org/10.1039/c9dt03974k.

[26] S. Wang, Y. Zou, F. Xu, C. Xiang, H. Peng, J. Zhang, L. Sun, Morphological control and electrochemical performance of NiCo2O4@NiCo layered double hydroxide as an electrode for supercapacitors, J. Energy Storage. 41 (2021) 102862. https://doi.org/10.1016/j.est.2021.102862.

[27] X. Xue, J. Zhong, J. Liu, Z. Hou, X. Wu, S. Li, M. Yu, Hydrolysis of metal-organic framework towards three-dimensional nickel cobalt-layered double hydroxide for high performance supercapacitors, J. Energy Storage. 31 (2020) 101649. https://doi.org/10.1016/j.est.2020.101649.

[28] A.G. El-Deen, M.K. Abdel-Sattar, N.K. Allam, High-performance solid-state supercapacitor based on Ni-Co layered double hydroxide@Co3O4 nanocubes and spongy graphene electrodes, Appl. Surf. Sci. 587 (2022) 152548. https://doi.org/10.1016/j.apsusc.2022.152548.

[29] J. Xu, H. Cao, C. Ni, Y. Wang, J. Cao, Z. Chen, Design and synthesis of sandwich-like CoNi 2 S 4 @C@NiCo-LDH microspheres for supercapacitors, J. Solid State Electrochem. (2019) 1513–1522. https://doi.org/10.1007/s10008-019-04246-0.

[30] R.S. Kate, S.A. Khalate, R.J. Deokate, Overview of nanostructured metal oxides and pure nickel oxide (NiO) electrodes for supercapacitors: A review, J. Alloys Compd. 734 (2018) 89–111. https://doi.org/10.1016/j.jallcom.2017.10.262.

[31] S. Liu, D. Ni, H.F. Li, K.N. Hui, C.Y. Ouyang, S.C. Jun, Effect of cation substitution on the pseudocapacitive performance of spinel cobaltite MCo2O4 (M = Mn, Ni, Cu, and Co), J. Mater. Chem. A. 6 (2018) 10674–10685. https://doi.org/10.1039/c8ta00540k.

[32] S.S. Haider, M.Z. Iqbal, S. Zakar, A.M. Afzal, K. Yaqoob, S. Aftab, Superior performance of electrodeposited CoMnS as novel electrode material for supercapattery devices, J. Energy Storage. 39 (2021) 102608. https://doi.org/10.1016/j.est.2021.102608.

[33] A.G. Hassan, M.A.M. Yajid, S.N. Saud, T.A.A. Bakar, A. Arshad, N. Mazlan, Effects of varying electrodeposition voltages on surface morphology and corrosion behavior of multi-walled carbon nanotube coated on porous Ti-30 at.%-Ta shape memory alloys, Surf. Coatings Technol. 401 (2020). https://doi.org/10.1016/j.surfcoat.2020.126257.

[34] X. Wang, X. Li, Q. Zhang, Z. Lu, H. Song, Y. Wang, Electrodeposition of ZnO Nanorods with Synergistic Photocatalytic and Self-Cleaning Effects, J. Electron. Mater. 50 (2021) 4954–4961. https://doi.org/10.1007/s11664-021-08958-w.

[35] D. George, A. Garcia, Q. Pham, M.R. Perez, J. Deng, M.T. Nguyen, T. Zhou, S.O. Martinez-Chapa, Y. Won, C. Liu, R.C. Lo, R. Ragan, M. Madou, Fabrication of patterned graphitized carbon wires using low voltage near-field electrospinning, pyrolysis, electrodeposition, and chemical vapor deposition, Microsystems Nanoeng. 6 (2020). https://doi.org/10.1038/s41378-019-0117-7.

[36] M. Zhang, Y. Chen, D. Yang, J. Li, High performance MnO2 supercapacitor material prepared by modified electrodeposition method with different electrodeposition voltages, J. Energy Storage. 29 (2020). https://doi.org/10.1016/j.est.2020.101363.

[37] A. Yavuz, P. Yilmaz Erdogan, N. Ozdemir, H. Zengin, G. Zengin, M. Bedir, Effect of cathodic deposition potential on the performance of nanostructured cobalt-based film for asymmetric supercapacitor fabrication, Solid State Sci. 99 (2020) 106074. https://doi.org/10.1016/j.solidstatesciences.2019.106074.

[38] A.K. Yedluri, H.J. Kim, Wearable super-high specific performance supercapacitors

using a honeycomb with folded silk-like composite of NiCo2O4 nanoplates decorated with NiMoO4 honeycombs on nickel foam, Dalt. Trans. 47 (2018) 15545–15554. https://doi.org/10.1039/c8dt03598a.

[39] D.K. Kulurumotlakatla, A.K. Yedluri, H.J. Kim, Hierarchical NiCo2S4 nanostructure as highly efficient electrode material for high-performance supercapacitor applications, J. Energy Storage. 31 (2020) 101619. https://doi.org/10.1016/j.est.2020.101619.

[40] Y. Anil Kumar, H.J. Kim, Preparation and electrochemical performance of NiCo2O4@NiCo2O4 composite nanoplates for high performance supercapacitor applications, New J. Chem. 42 (2018) 19971–19978. https://doi.org/10.1039/c8nj05401k.

[41] G. Rutavi, D.J. Tarimo, V.M. Maphiri, N. Manyala, Two-step electrodeposition of Hausmannite sulphur reduced graphene oxide and cobalt-nickel layered double hydroxide heterostructure for high-performance supercapacitor, Int. J. Energy Res. (2022) 1–14. https://doi.org/10.1002/er.7922.

[42] Y. Anil Kumar, S. Singh, D.K. Kulurumotlakatla, H.J. Kim, A MoNiO4 flower-like electrode material for enhanced electrochemical properties: Via a facile chemical bath deposition method for supercapacitor applications, New J. Chem. 44 (2019) 522–529. https://doi.org/10.1039/c9nj05529k.

[43] Y. Anil Kumar, K. Dasha Kumar, H.J. Kim, Facile preparation of a highly efficient NiZn2O4-NiO nanoflower composite grown on Ni foam as an advanced battery-Type electrode material for high-performance electrochemical supercapacitors, Dalt. Trans. 49 (2020) 3622–3629. https://doi.org/10.1039/d0dt00268b.

[44] Y.S. Lee, Y.A. Kumar, S. Sambasivam, S.A. Hira, K. Zeb, W. Uddin, P.R.S. Reddy, K.D. Kumar, I.M. Obaidat, H.J. Kim, S. Kim, CoCu2O4 nanoflowers architecture as

an electrode material for battery type supercapacitor with improved electrochemical performance, Nano-Structures and Nano-Objects. 24 (2020) 100618. https://doi.org/10.1016/j.nanoso.2020.100618.

[45] D.J. Tarimo, A.A. Mirghni, K.O. Oyedotun, G. Rutavi, V.N. Kitenge, N. Manyala, Recycling of biomass wastes from amarula husk by a modified facile economical water salt method for high energy density ultracapacitor application, J. Energy Storage. 53 (2022) 105166. https://doi.org/10.1016/j.est.2022.105166.

[46] J. Barman, S. Ravi, Effect of Al Substitution in Structural and Magnetic Properties of MnCr2O4, J. Supercond. Nov. Magn. 31 (2018) 99–106. https://doi.org/10.1007/s10948-017-4169-3.

[47] R.A. Sanguramath, B. Laadan, N. Raz, A. Katalan, D.J. Benarroch, A. Franco, CuO(1−x)ZnOx nanocomposite with broad spectrum antibacterial activity: Application in medical devices and acrylic paints, Nanotechnology. 32 (2021). https://doi.org/10.1088/1361-6528/abe826.

[48] N. Zhao, H. Fan, M. Zhang, C. Wang, X. Ren, H. Peng, H. Li, X. Jiang, X. Cao, Preparation of partially-cladding NiCo-LDH/Mn3O4 composite by electrodeposition route and its excellent supercapacitor performance, J. Alloys Compd. 796 (2019) 111–119. https://doi.org/10.1016/j.jallcom.2019.05.023.

[49] Q. Hu, W. Li, B. Xiang, X. Zou, J. Hao, M. Deng, Q. Wu, Y. Wang, Sulfur source-inspired synthesis of β-NiS with high specific capacity and tunable morphologies for hybrid supercapacitor, Electrochim. Acta. 337 (2020) 135826. https://doi.org/10.1016/j.electacta.2020.135826.

[50] S. Sarkar, R. Akshaya, S. Ghosh, Nitrogen doped graphene/CuCr2O4 nanocomposites for supercapacitors application: Effect of nitrogen doping on coulombic efficiency,

Electrochim. Acta. 332 (2020) 135368. https://doi.org/10.1016/j.electacta.2019.135368.

[51] P. Mani, V. Vellaikasi, X.T. Suryabai, A.R. Simon, T. Kattaiyan, Cubic like CoMn 2 O 4 nanostructures as advanced high-performance pseudocapacitive electrode, 00 (2022) 1–10.

[52] L. Li, K.S. Hui, K.N. Hui, Y.R. Cho, Ultrathin petal-like NiAl layered double oxide/sulfide composites as an advanced electrode for high-performance asymmetric supercapacitors, J. Mater. Chem. A. 5 (2017) 19687–19696. https://doi.org/10.1039/c7ta06119f.

[53] S. Saini, P. Chand, Effect of aqueous electrolytes on h-WO3 nanorods as an electrode material for supercapacitor application, Chem. Phys. Lett. 802 (2022) 139760. https://doi.org/10.1016/j.cplett.2022.139760.

[54] A. Raghavan, S. Sarkar, S. Ghosh, Dnevelopment of PANI based ternary nanocomposite with enhanced capacity retention for high performance supercapacitor application, Electrochim. Acta. 388 (2021) 138564. https://doi.org/10.1016/j.electacta.2021.138564.

[55] S. Acharya, S. Sahoo, S. Sonal, J.H. Lee, B.K. Mishra, G.C. Nayak, Adsorbed Cr(VI) based activated carbon/polyaniline nanocomposite: A superior electrode material for asymmetric supercapacitor device, Compos. Part B Eng. 193 (2020) 107913. https://doi.org/10.1016/j.compositesb.2020.107913.

[56] M. Guo, Y. Liu, F. Zhang, F. Cheng, C. Cheng, Y. Miao, F. Gao, J. Yu, Inactive Al3+-doped La(CoCrFeMnNiAlx)1/(5+x)O3 high-entropy perovskite oxides as high performance supercapacitor electrodes, c (2022) 742–753.

[57] Q. Zhou, J. Wang, R. Zheng, Y. Gong, J. Lin, One-step mild synthesis of Mn-based spinel MnIICrIII2O4/MnIIMnIII2O4/C and Co-based spinel CoCr2O4/C nanoparticles as battery-type electrodes for high-performance supercapacitor application, Electrochim. Acta. 283 (2018) 197–211. https://doi.org/10.1016/j.electacta.2018.06.164.

[58] S. Maitra, R. Mitra, T.K. Nath, Sol-gel derived MgCr2O4 nanoparticles for aqueous supercapacitor and alkaline OER and HER bi-functional electrocatalyst applications, J. Alloys Compd. 858 (2021) 157679. https://doi.org/10.1016/j.jallcom.2020.157679.

[59] A. Farisabadi, M. Moradi, S. Borhani, S. Hajati, M.A. Kiani, S.A. Tayebifard, Synthesis and electrochemical properties of Mg-doped chromium-based metal organic framework/reduced graphene oxide composite for supercapacitor application, J. Mater. Sci. Mater. Electron. 29 (2018) 8421–8430. https://doi.org/10.1007/s10854-018-8853-2.

[60] I. Shafi, E. Liang, B. Li, Ultrafine chromium oxide (Cr2O3) nanoparticles as a pseudocapacitive electrode material for supercapacitors, J. Alloys Compd. 851 (2021). https://doi.org/10.1016/j.jallcom.2020.156046.

[61] Z. Chen, H. Deng, M. Zhang, Z. Yang, D. Hu, Y. Wang, K. Yan, One-step facile synthesis of nickel-chromium layered double hydroxide nanoflakes for high-performance supercapacitors, Nanoscale Adv. 2 (2020) 2099–2105. https://doi.org/10.1039/d0na00178c.

[62] M.D. Najafi, E. Kowsari, H.R. Naderi, A. Chinnappan, S. Ramakrishna, A. Ehsani, A. Shokravi, Functionalization of graphene oxide via chromium complexes coordinated on 5-aminopyridine-2-carboxylic acid as a symmetric supercapacitor electrode materials in energy storage devices, Compos. Sci. Technol. 211 (2021) 108844.

https://doi.org/10.1016/j.compscitech.2021.108844.

[63] A.A. Mirghni, K.O. Oyedotun, B.A. Mahmoud, O. Fasakin, D.J. Tarimo, N. Manyala, A study of Co-Mn phosphate supported with graphene foam as promising electrode materials for future electrochemical capacitors, Int. J. Energy Res. 46 (2022) 3080–3094. https://doi.org/10.1002/er.7365.

[64] D.J. Tarimo, K.O. Oyedotun, A.A. Mirghni, B. Mutuma, N.F. Sylla, P. Murovhi, N. Manyala, Enhanced electrochemical performance of supercapattery derived from sulphur-reduced graphene oxide/cobalt oxide composite and activated carbon from peanut shells, Int. J. Hydrogen Energy. 45 (2020) 33059–33075. https://doi.org/10.1016/j.ijhydene.2020.09.142.

[65] A.M. Abuelftooh, N.S. Tantawy, S.S. Mahmouad, M.A. Shoeib, S.G. Mohamed, High specific energy supercapacitor electrode prepared from MnS/Ni3S2composite grown on nickel foam, New J. Chem. 45 (2021) 18641–18650. https://doi.org/10.1039/d1nj03930j.

[66] S. Sarr, N.F. Sylla, D.T. Bakhoum, K.O. Oyedotun, B.D. Ngom, N. Manyala, Effect of neutral electrolytes on vanadium dioxide microspheres-based electrode materials for asymmetric supercapacitors, J. Energy Storage. 43 (2021) 103294. https://doi.org/10.1016/j.est.2021.103294.

[67] R. Shafique, M. Rani, A. Mahmood, R.A. Alshgari, K. Batool, T. Yaqoob, N.K. Janjua, S. Khan, S. Khan, G. Murtaza, Investigations of 2D Ti3C2(MXene)-CoCr2O4 nanocomposite as an efficient electrode material for electrochemical supercapacitors, Int. J. Energy Res. 46 (2022) 6689–6701. https://doi.org/10.1002/er.7605.

[68] Q. Li, J. Zhou, S. Zhao, Y. Li, C. Chen, K. Tao, R. Liu, L. Han, Hollow and Hierarchical Cobalt–Metal Organic Framework@CoCr2O4 Microplate Array as a

Battery-Type Electrode for High-Performance Hybrid Supercapacitors, ChemElectroChem. 7 (2020) 437–444. https://doi.org/10.1002/celc.201902015.

[69] Y. Hai, K. Tao, H. Dan, L. Liu, Y. Gong, Cr-doped (Co, Ni)3S4/Co9S8/Ni3S2 nanowires/nanoparticles grown on Ni foam for hybrid supercapacitor, J. Alloys Compd. 835 (2020) 155254. https://doi.org/10.1016/j.jallcom.2020.155254.

[70] G.G. Soundarya, B. Nalini, D. Lakshmi, P. Priyanka, Structural rearrangement by Ni, Cr doping in zinc cobaltite and its influence on supercapacitance, Ceram. Int. 47 (2021) 18635–18645. https://doi.org/10.1016/j.ceramint.2021.03.195.

[71] A. Chowdhury, S. Biswas, T. Singh, A. Chandra, Redox mediator induced electrochemical reactions at the electrode-electrolyte interface: Making sodium-ion supercapacitors a competitive technology, Electrochem. Sci. Adv. 2 (2022) 1–14. https://doi.org/10.1002/elsa.202100030.

[72] Y. He, D. Liu, H. Zhao, J. Wang, Y. Sui, J. Qi, Z. Chen, P. Zhang, C. Chen, D. Zhuang, Carbon-coated NiMn layered double hydroxides/Ni3S2 nanocomposite for high performance supercapacitors, J. Energy Storage. 41 (2021) 103003. https://doi.org/10.1016/j.est.2021.103003.

[73] Y.X. Zhu, G.L. Song, P.P. Wu, D.J. Zheng, Z.M. Wang, A burnished and Al-alloyed magnesium surface with improved mechanical and corrosion properties, Corros. Sci. 184 (2021) 109395. https://doi.org/10.1016/j.corsci.2021.109395.

[74] H. Liu, M. Dai, D. Zhao, X. Wu, B. Wang, Realizing Superior Electrochemical Performance of Asymmetric Capacitors through Tailoring Electrode Architectures, ACS Appl. Energy Mater. 3 (2020) 7004–7010. https://doi.org/10.1021/acsaem.0c01055.

[75] M. Haque, Q. Li, A.D. Smith, V. Kuzmenko, P. Rudquist, P. Lundgren, P. Enoksson, Self-discharge and leakage current mitigation of neutral aqueous-based supercapacitor by means of liquid crystal additive, J. Power Sources. 453 (2020). https://doi.org/10.1016/j.jpowsour.2020.227897.

[76] G. Rutavi, D.J. Tarimo, V.M. Maphiri, V.N. Kitenge, N. Manyala, Exploration of metal-layered double hydroxide composite material for hybrid capacitor produced by facile and efficient electrodeposition process, J. Alloys Compd. 929 (2022) 167216. https://doi.org/10.1016/j.jallcom.2022.167216.

[77] V.M. Maphiri, D.T. Bakhoum, S. Sarr, N.F. Sylla, G. Rutavi, N. Manyala, Low temperature thermally reduced graphene oxide directly on Ni-Foam using atmospheric pressure-chemical vapour deposition for high performance supercapacitor application, J. Energy Storage. 52 (2022) 104967. https://doi.org/10.1016/j.est.2022.104967.

[78] R. Ghanbari, M. Entezar Shabestari, E. Naderi Kalali, Y. Hu, S.R. Ghorbani, Electrochemical performance and complex impedance properties of reduced-graphene oxide/polypyrrole nanofiber nanocomposite, Ionics (Kiel). 27 (2021) 1279–1290. https://doi.org/10.1007/s11581-021-03907-3.

[79] M.N. Rantho, M.J. Madito, F.O. Ochai-Ejeh, N. Manyala, Asymmetric supercapacitor based on vanadium disulfide nanosheets as a cathode and carbonized iron cations adsorbed onto polyaniline as an anode, Electrochim. Acta. 260 (2018) 11–23. https://doi.org/10.1016/j.electacta.2017.11.074.